



Mitigation of shock loading on structures using aqueous methylcellulose solution



Koray Senol^a, Galit Parvari^b, Yonatan Rotbaum^c, Yoav Eichen^b, Daniel Rittel^c, Arun Shukla^{a,*}

^a Department of Mechanical, Industrial and Systems Engineering, University of Rhode Island, Kingston, RI 02881, USA

^b Schulich Faculty of Chemistry, Technion– Israel Institute of Technology, 3200008 Haifa, Israel

^c Faculty of Mechanical Engineering, Technion – Israel Institute of Technology, 3200008 Haifa, Israel

ARTICLE INFO

Keywords:

Aqueous methylcellulose
Thermoreversible gelation
Digital image correlation
Shock loading
Energy mitigation

ABSTRACT

Shock mitigation performance of aqueous methylcellulose hydrogel and water for structural applications was investigated through two dynamic loading instruments: Instrumented bar and shock tube. While aqueous methylcellulose solutions have previously been found to attenuate impact-induced forces passing through them by a unique liquid-to-solid phase transition, this is the first time studied as shock mitigators to structural elements. The results obtained with aqueous methylcellulose as mitigator were compared with an equivalent experiment conducted with water as damping medium. The liquid was loaded into a specially designed hollow aluminum box, built to allow transmission of dynamic stress waves to a thin back plate. Determination of the liquid's attenuation performance was based on the 3D Digital Image Correlation technique with high-speed photography to obtain the full-field real-time deformation data of the back-face plate throughout the dynamic loading event. It was found that upon high rate loading with the instrumented bar, the aqueous methylcellulose solution decreases the maximum out of plane displacement resulting from the dynamic loading by as much as 40% compared to water, and significantly damps the structural vibrations of the back-face plate. On the other hand, upon relatively low rate loading with shock tubes, water and aqueous methylcellulose solutions provide the same magnitude of out of plane displacement, however, the damping ratio (Logarithmic Decrement) of the structure through aqueous methylcellulose solutions is 45% greater than through water. The findings are analyzed and rationalized in terms of imparted mechanical power.

1. Introduction

Many engineering structures are designed to perform under extreme conditions such as high accelerations, vibrations, or even strong impacts, all of which might jeopardize the whole device or sub-modules within it [1–3]. For instance, during takeoff or sharp maneuvers, drones experience high accelerations which often lead to repeating malfunctions in electronic circuits [4,5]. To protect the electronic devices, the circuits are molded inside a protective polymer or in a cushioned case [6,7]. Similarly, wave slamming and hard landings onto water surfaces challenge the structural integrity of naval crafts and racing boats on a daily basis [8–12]. Land vehicles are also equipped with the proper suspensions and shock absorbers to isolate the passengers and mechanical apparatus from the vibrations caused by a bumpy road and further, for protection from accidents [13,14]. Nowadays, there are many available products and techniques designed to ensure the integrity of a structure subjected to violent loading conditions. Among

these, one can find collapsing metallic foams [15,16], honeycombs, polymeric layers [17,18], and floating devices. Upon loading, the above-mentioned elements cushion the device from the impact, and a portion of the transferred elastic energy is reflected, dispersed, or absorbed [19].

However, while most of the mentioned solutions provide efficient protection from structural penetration and eventual fracture, they do not efficiently damp the initial violent elastic accelerations that could, among other things, cause traumatic organ injury. Therefore, research has to be invested in finding solutions that mitigate those violent accelerations, alongside more conventional protection solutions.

Hydrogels have received significant attention in the past few decades due to their wide range of applications in fields including agriculture, drug delivery systems, food additives, pharmaceuticals, biomedical applications, tissue engineering, and wound dressing [20–26]. Aqueous methylcellulose solutions (AMCS) form hydrogels thermo-reversibly [27,28], and have a wide range of applications, similar to other

* Corresponding author.

E-mail address: shuklaa@uri.edu (A. Shukla).

<https://doi.org/10.1016/j.ijimpeng.2020.103547>

Received 13 December 2019; Received in revised form 6 February 2020; Accepted 24 February 2020

Available online 25 February 2020

0734-743X/ © 2020 Elsevier Ltd. All rights reserved.

hydrogels [29–32]. More recently, AMCSs were reported to undergo impact-induced gelation [33]. These materials, which were known for decades to endothermically transition to a gel upon heating [34,35] or exposure to large pressures [36,37] were shown to respond quite rapidly (within microseconds) to impact, and significantly reduce the amplitudes of forces passing through them following impact. These force reductions were compared to those of ballistic gelatin and water, and were significantly larger for AMCS than either of these two materials. In addition, compositing methylcellulose (MC) hydrogels with various particles leads to the tailoring of their flow stresses [38]. Finally, the shock attenuation performance of AMCS as a function of concentration and thickness was also recently studied [39].

However, the influence of AMCS on structural dynamics has not yet been investigated. The purpose of the present work is to investigate the structural shock mitigation by AMCS under different dynamic loading scales, including an instrumented bar in a microseconds loading duration and shock tube in a milliseconds loading duration. The performance of AMCS is compared to that of water, which is the main component (>94% weight) of AMCS. In the first part, an instrumented bar setup (modified from a traditional SHPB for compressive loadings) was used to generate the dynamic loading on a specially designed aluminum (Al) frame filled by liquid AMC or water [40,41]. 3D Digital Image Correlation (DIC) technique was used with high-speed photography to obtain the full-field deformation data throughout the dynamic loading event [11,42–44]. In the second part, a shock tube apparatus and 3D DIC were used to generate and analyze the blast-analog loading effect on a similar structure with polycarbonate (PC) face sheets filled with those liquids [17,45,46]. These two apparatuses enable different dynamic loading rates of the AMCS in order to analyze the importance of this parameter on the material's attenuation performance.

2. Experimental procedures

2.1. Materials and specimen dimensions

An Al 6061 fixture for instrumented bar experiments was manufactured to store liquid fillers (see Fig. 1). The fixture consists of a square-shaped front face Al plate ($216 \times 216 \times 13$ mm), four solid Al square bars (25×25 mm cross section), twenty $\frac{1}{2}$ –13 bolt - nut sets, and a square shape Al back face plate ($216 \times 216 \times 0.8$ mm). Bolts are positioned 38 mm on centers with 35 mm steel washers to ensure uniform fixed boundary conditions. A similar fixture for shock tube experiments was used by replacing the Al front and back face plates with PC front ($216 \times 216 \times 13$ mm) and back ($216 \times 216 \times 0.8$ mm) face plates. Table 1 provides some mechanical properties of Al and PC materials used in this study. The fixtures were sealed with silicone sealant to prevent any liquid leaking from the fixtures during dynamic loading. The liquid filler volume available in the fixtures was 0.7 L. Tap water and AMCS with a 5.6% wt. (56 g/L) concentration were used as liquid fillers in this study. The configuration of each specimen used in each experiment is presented in Fig. 1 for (a) instrumented bar and (b) shock tube. It should be noted that in some cases the face sheets are reused to ensure consistency of the experimental setup. This is viable because in plane strains are always well within the elastic limits of both Al and PC face sheets.

Methocel SG A7C food grade (Dow Chemicals Inc.) powder was used in this study to prepare the AMCS. 28 g of the methylcellulose powder was added to 0.25 L purified water heated to 75 °C, and mixed well until a uniformly opaque dispersion was obtained. Then, 0.25 L purified water at 5 °C was added and the solution was mixed well until a uniform dispersion of 0.5 L was obtained. Afterwards, the solution at 56 g/L concentration was placed in an ice bath for 2 h until the solution turned transparent and homogenous. The solution was then kept in a refrigerator for 24 h at 3–5 °C. Finally, 0.7 L of 1 L AMC solution (prepared in two 0.5 L beakers) was poured into the hollow Al box and allowed to reach room temperature for the dynamic loading

experiments. A schematic representation of the manufacturing process for AMCS is presented in Fig. 2.

2.2. Dynamic loading facility

An instrumented bar setup (modified from a SHPB (Kolsky) setup for compressive loading) was used to perform dynamic loading experiments [47,48]. The loading steel bar has a diameter of 51 mm and a length of 4880 mm. Two diametrically opposite strain gages (Model: C2A-13–250LW-350 from Vishay Precision Group, Inc.) were cemented on the incident bar, 1220 mm from the specimen's front face which recorded the incident and reflected pulses at a 1 MHz sampling rate. The dynamic stress wave was created by firing an Al projectile from a gas gun. Once the striker hits the loading bar, a compressive stress wave propagates along the loading bar and reaches the end of the bar where the Al front face plate is in contact with the loading bar. At this instant, part of the stress wave propagates further through the 13 mm thick Al front face plate, the 25 mm liquid filler, then reaching the 0.8 mm Al back face plate, while the other part reflects back in the loading bar as a tensile wave.

For the other set of experiments, a shock tube setup was used to perform shock loading experiments. The shock tube muzzle has an inner diameter of 38 mm. Three dynamic pressure sensors were located 20 mm, 60 mm and 180 mm from the specimen's front face and sampled at 5 MHz. The shock loading was created by bursting a diaphragm due to pressure difference between high (driver) and low-pressure (driven) sections separated by the diaphragm. Once the diaphragm bursts, a rapid expansion of the compressed gas creates a shock wave that travels towards the open muzzle end. At this instant of shock wave's muzzle exit, part of the shock wave propagates further through the 13 mm PC front face plate and the 25 mm liquid filler then reaching the 3.2 mm PC back face plate, while the other part of the shock wave reflects back into the shock tube muzzle. It is to be noted that the configuration of the apparatus was similar for both instrumented bar and shock tube experiments except for the materials of the front face plates and the materials and thicknesses of the back-face plates. The reason for changing the material of the face plates for the shock tube experiments was to decrease the impedance mismatch between the shock medium, the front and back-face plates and filler liquids. As a result, a sufficient amount of the incident energy can be transmitted through the back-face plate resulting in large enough displacements on the back-face plate.

Two Photron SA1 (Photron USA, Inc.) high-speed cameras with two high intensity light sources were used to record the real-time deformation response of the Al/PC back face through 3D DIC technique. These cameras are used at a resolution of 320×512 pixels at 30,000 frames per second, yielding an optical resolution of 26 μ m. 3D-DIC technique is a well-known non-contact method for full-field displacement measurements [42]. Image processing and data reduction were performed using VIC-3D 7 software (Correlated Solutions, Inc. Columbia, SC). Each black speckle generated for DIC application was ensured to occupy at least 3 by 3 pixels (giving a minimum of 78 μ m speckle diameter). Subset and step sizes in VIC software were selected to be 21 and 7 pixels, respectively. Moreover, the strain calculations in VIC software were filtered through the Lagrange tensor type with a filter size of 15. This gives a total smoothing area of 105 pixels (7 step \times 15 filter size). In other words, the size of the virtual strain gage used in strain calculations is 105. Figs. 3 and 4 present detailed schematics of the instrumented bar and shock tube setups, respectively.

3. Experimental results

3.1. Part A - instrumented bar

The dynamic loading experiments were conducted using the instrumented bar setup shown in Fig. 3. Incident and reflected strain pulses were recorded by an oscilloscope while the real-time out of plane

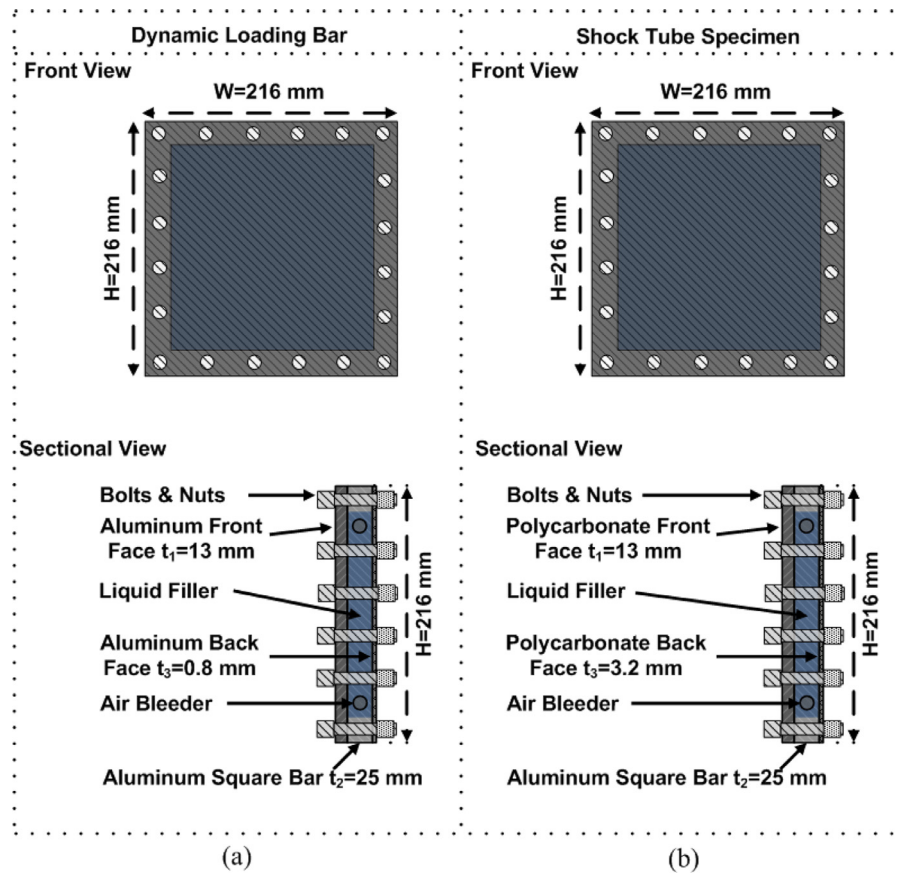


Fig. 1. A scheme of the specimen used in (a) instrumented bar and (b) shock tube experiments.

Table 1

Mechanical properties of aluminum and polycarbonate sheets used in this study.

| Material | Young's Modulus (GPa) | Yield Strength (MPa) | Ultimate Tensile Strength (MPa) |
|---------------|-----------------------|----------------------|---------------------------------|
| Aluminum | 69 | 240 | 290 |
| Polycarbonate | 2.2 | 63 | 70 |

displacement of the back-face plate was recorded through two high speed cameras also used for 3D DIC application. Four loading trials through different impulse inputs were carried out for each liquid filler case in the instrumented bar setup. Fig. 5 summarizes the out of plane displacement history of the center point of the back-face plate with water (black curve) and AMC (red curve) fillers. Here the out of plane displacement is denoted by W , and the center point is the location where the maximum value of W occurred on the full field. It is seen from Fig. 5 that the center point vibrates over the reference plane coordinate in each loading case for both water and AMC. However, the damping of the vibration by AMC filler is always stronger than water filler regardless of the W_{\max} occurred as seen in Fig. 5. For instance, even though W_{\max} values in Water #3 and AMC #4 experiments are equal, the damping of the W by AMC filler is significantly stronger than water filler. This better mitigation performance (energy intake) of AMC over water is due to its local endothermic gelation resulting from shock loading [33]. More details on impact-induced gelation of AMC can be found in [33].

For a representation of the input-output correlation of each experiment, W_{\max} as a function of the input impulse data is presented in Fig. 6. The impulse given in Fig. 6 was obtained by the integration of the input force with respect to time, and this net input force history

applied onto the specimen was obtained by the subtraction of the reflected pulse from the incident pulse. As seen in Fig. 6, W_{\max} through the water filler is always larger than W_{\max} through the AMC filler for a given impulse.

Two cases of each liquid were selected for more detailed analysis. These two cases were selected by considering similar input impulses for each liquid. Experiments in Case #1 were selected to be Water #3 and AMC #3 while they in Case #2 were selected to be Water #4 and AMC #4 (see Fig. 5 for experiment numbers). The input impulses are 1.4 N·s for both Case#1-water and Case#1-AMC, while they are 1.8 N·s and 1.7 N·s for Case#2-water and Case#2-AMC, respectively. Water and AMC fillers in Case #1 will be denoted as Water-A-1.4 and AMC-A-1.4, while they in Case#2 will be denoted as Water-A-1.8 and AMC-A-1.7, respectively. "A" refers to Part-A, which means that the experiment belongs to the instrumented bar setup while the following number in the denotation refers to the applied impulse to point the respective case. The absolute values of the incident and reflected pulse histories for the experiments Water-A-1.4 and AMC-A-1.4 in Case#1, and Water-A-1.8 and AMC-A-1.7 in Case#2 are presented in Fig. 7. It is seen from Fig. 7 that the incident and reflected pulses in each liquid case are similar despite some differences in terms of peak values for both Case#1 and Case#2. Though pulses for AMC display larger peak values, this offset is maintained in both incident and reflected pulses so that the net force remains similar in magnitude to the water case. In Case#1, the peak values of the incident pulses are 130 and 150 kN while the peak values of the reflected pulses are 100 and 110 kN for Water-A-1.4 and AMC-A-1.4, respectively. Moreover, in Case#2, the peak values of the incident pulses are 180 and 190 kN while the peak values of the reflected pulses are 130 and 140 kN for Water-A-1.8 and AMC-A-1.7 fillers, respectively.

The net force acting on the structure can be obtained by addition of the magnitudes of the incident and reflected pulses given in Fig. 7.

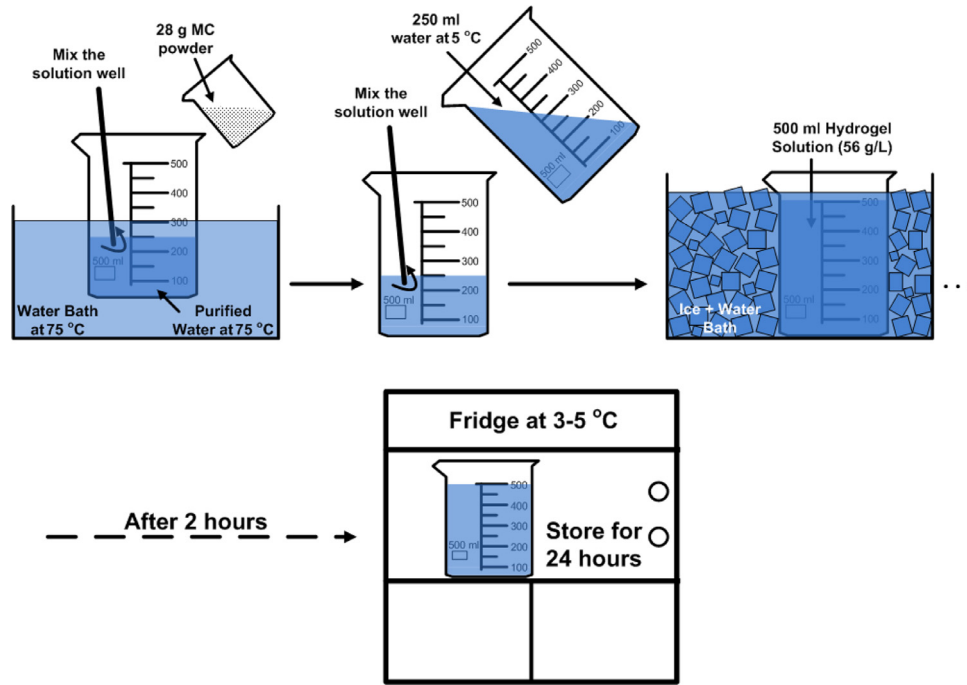


Fig. 2. Schematic representation of the manufacturing process of 0.5 L of AMCS.

Those net forces are presented in Fig. 8 for (a) Water-A-1.4, (b) AMC-A-1.4, (c) Water-A-1.8 and (d) AMC-A-1.7. The input impulses can also be obtained by the integration of the net input force with respect to time given in Fig. 8. The input impulses are 1.4 N·s for both Case#1-water and Case#1-AMC, while they are 1.8 N·s and 1.7 N·s for Case#2-water and Case#2-AMC, respectively.

The out of plane displacement data for these two cases obtained by 3D DIC technique is shown in Fig. 9. In the first row of Fig. 9, $t = 0$ is the instant when the stress wave reaches the front-face plate of the specimen (no loading yet on the specimen). In the second row, time 1.0 ms is the instant when the maximum out of plane displacement

occurs on the back-face plate due to the dynamic loading. It is seen from those images that full-field out of plane displacements for both Water-A-1.4 and Water-A-1.8 are significantly larger than AMC-A-1.4 and AMC-A-1.7 respectively, indicating better mitigation of the dynamic load through AMC. The third row (time = 2 ms) shows the instant when the minimum out of plane displacement occurs on the back-face plates for each loading case. Finally, the last row (time = 25 ms) shows the final stages captured through 3D DIC for each loading case where the out of plane displacements are almost zero for all cases.

The evolution of out of plane displacement data for a vertical line drawn along the center of the back-face plate (membrane) is presented

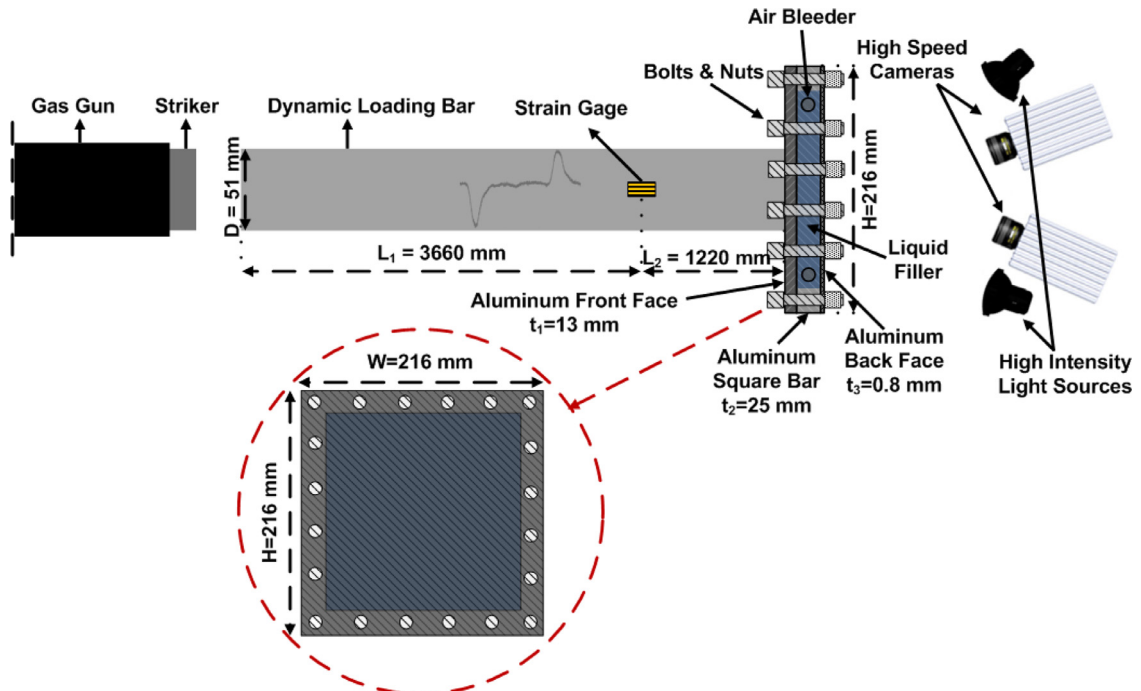


Fig. 3. A detailed schematic of the instrumented bar setup showing the gas gun, striker, dynamic loading bar, specimen and the 3D DIC set-up.

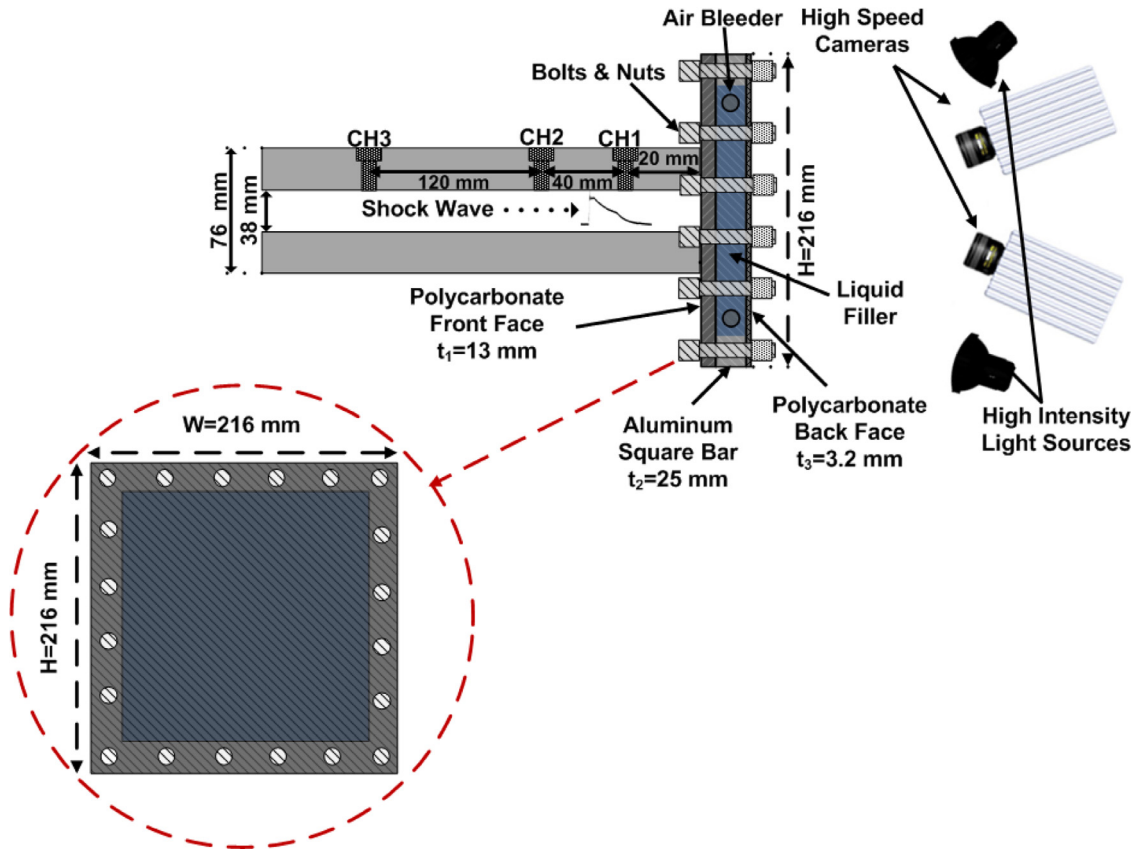


Fig. 4. A detailed schematic of the shock tube including the specimen and the 3D DIC setup. Structural configuration is similar to the instrumented bar setup except the PC front and back-face plates instead of Al front and back-face plates, and the thickness of the PC back-face plate (3.2 mm PC back face plate instead of 0.8 mm Al back-face plate).

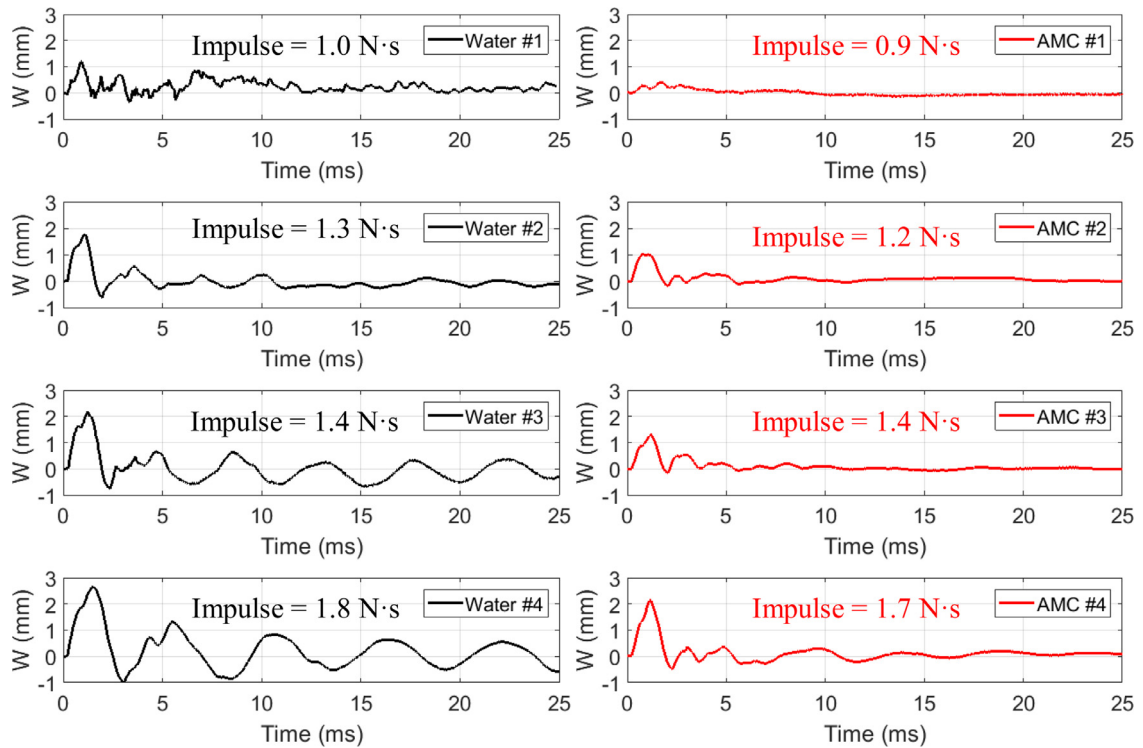


Fig. 5. The time variation of the real-time out of plane displacement data for the center point (where the maximum W occurs) of the back-face plate with water (black curve) and AMC (red curve) fillers for each trial. (For interpretation of the references to color in this figure legend, the reader is referred to the web version of this article.)

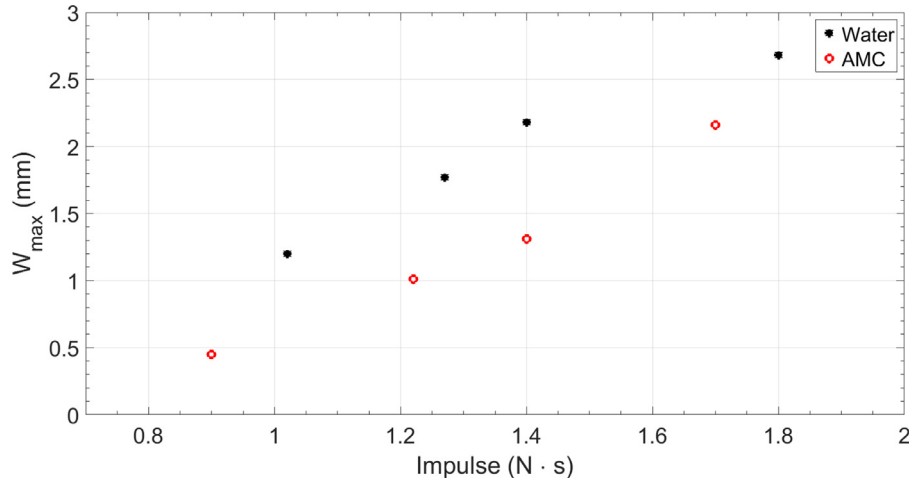


Fig. 6. The maximum out of plane displacement of the center point of the back face plate as a function of the input impulse applied onto the specimen.

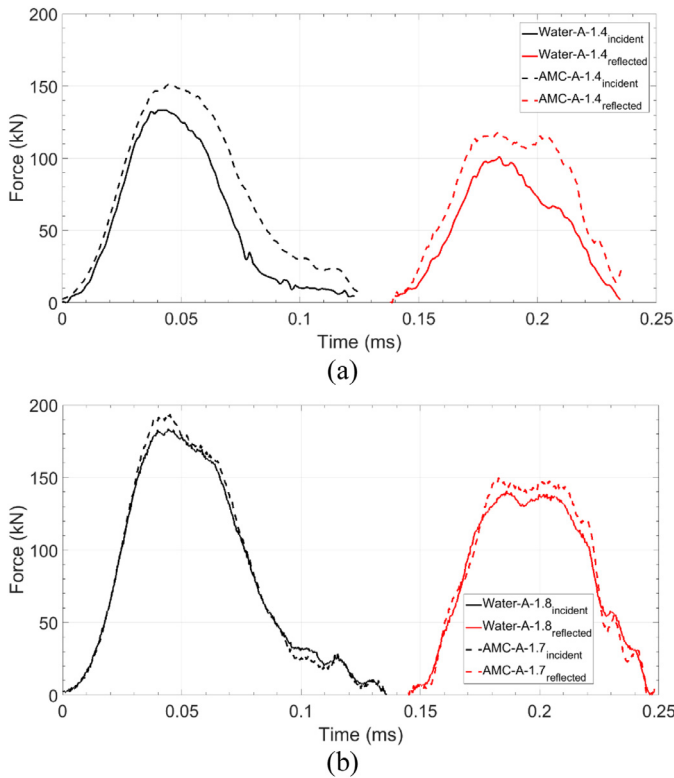


Fig. 7. The absolute values of the typical incident (black) and reflected (red) pulse histories for the experiments (a) Water-A-1.4 (solid curve) and AMC-A-1.4 (dashed curve), and (b) Water-A-1.8 (solid curve) and AMC-A-1.7 (dashed curve). (For interpretation of the references to color in this figure legend, the reader is referred to the web version of this article.)

in Fig. 10. It is seen from Fig. 10 that the out of plane displacement profile along the vertical center line is a wavy and sharply peaked curve for water, while it shows a smoothly deflected curve for AMC for both Case#1 and #2. It is also seen in Fig. 10 that oscillations in the evolution of out of plane displacement of the vertical center line are damped down quicker for AMC than water. Moreover, discontinuous deformation profile is seen in Fig. 10 especially for water filler. This is attributed to the nonlinear free vibration of a considerably thin plate backing the liquid filler. The peak deformation of the center point is observed 1.2 ms after the dynamic load reaches the thin plate. This time delay is indicative that a nonlinear vibration is being setup in the water domain which is causing the discontinuous deformation profile.

The thickness of the Al back face plate was 0.8 mm. Considering the back-face plate as a thin plate deforming in membrane mode, the strain energy U of the elastically deforming plate is given by [49]

$$U = V \frac{E}{2(1 - \nu^2)} (\varepsilon_1^2 + \varepsilon_2^2 + 2\nu\varepsilon_1\varepsilon_2) \quad (1)$$

where V is the volume of the back-face plate, E is Young's modulus, ν is Poisson's ratio, and ε_1 and ε_2 are the principal strains at any location on the full-field back-face plate surface. The 3D DIC provides real-time full-field principal strain data with a resolution of $\pm 100 \mu\epsilon$. The strain values recorded for all the experiments are in the order $\pm 1000 \mu\epsilon$. It is to be noted that among all the experiments conducted in the instrumented bar setup, the maximum principal strain on the Al back-face sheet was 0.18% for Water-A-1.8, which is within the elastic limits.

The average instantaneous strain energy U of the full-field back face plate surface was calculated for each case, as shown in Fig. 11. Fig. 11 reveals that the maximum average full-field strain energy in Water-A-1.4 is +0.12 J while it is +0.08 J for AMC-A-1.4, which gives 33% improvement in the maximum average full-field strain energy by the use of AMC with respect to water. On the other hand, the maximum average full-field strain energy in Water-A-1.8 is +0.37 J while it is +0.28 for AMC-A-1.7, which gives 24% improvement in the maximum average full-field strain energy by the use of AMC. Table 2 summarizes the key data presented in this section. In Table 2, W_{\max} is the maximum out of plane displacement of the center point, while U_{\max} is the maximum average full-field strain energy.

3.2. Part B - shock tube

The shock loading experiments were conducted using the shock tube setup shown in Fig. 4. Pressure pulses were recorded by an oscilloscope while the real-time out of plane displacement of the back-face plate was recorded through two high speed cameras for 3D DIC application. Real-time pressure data collected from CH1-3 (see Fig. 4) is presented in Fig. 12. It is seen in Fig. 12 that loading profiles are similar for each loading case. The peak pressures from CH1s are in the range of 5.5–5.9 MPa for both liquids and loading cases. Water and AMC fillers in Case #1 will be denoted as Water-B-14.5 and AMC-B-14.8 while they in Case#2 will be denoted as Water-B-14.2 and AMC-B-14.7, respectively. “B” refers to Part-B, which means the experiment belongs to the shock tube setup while the following number in the denotation refers to the applied impulse to point the respective case. It is also demonstrated in Fig. 12 that there is a secondary loading starting at around 13 ms due to the reflection of the incident shock wave from the closed end of the 7.5 m long shock tube. Impulse presented in Fig. 12 was calculated through the integral of the incident force (obtained via given pressure

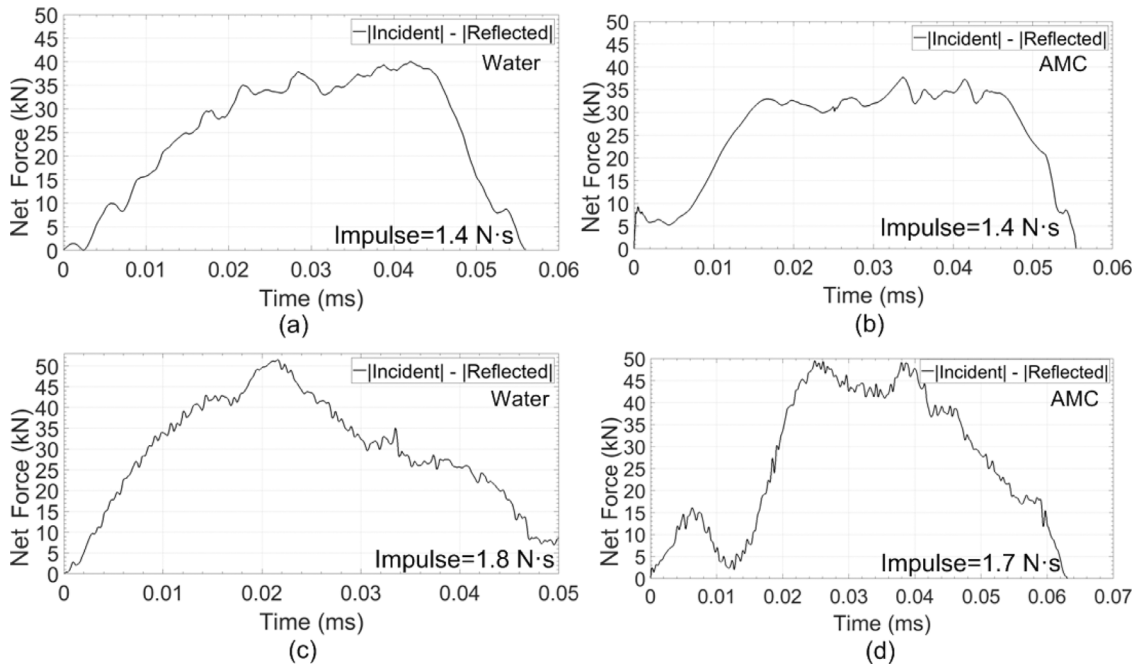


Fig. 8. The net forces acting on the specimen during the dynamic loading is obtained by addition of the reflected pulse with the (negative) incident pulse (Case #1: (a) Water-A-1.4 and (b) AMC-A-1.4; Case #2: (c) Water-A-1.8 and (d) AMCS-A-1.7).

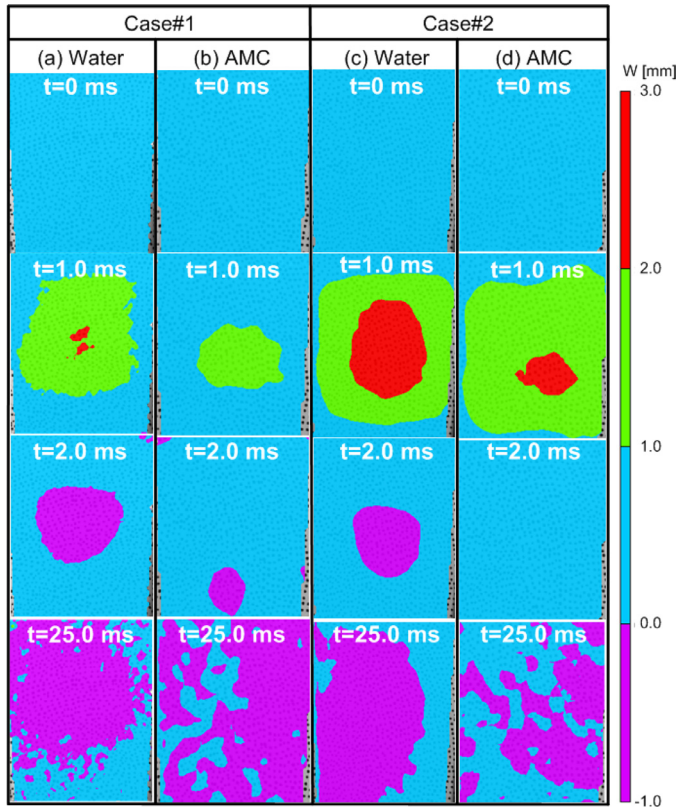


Fig. 9. The real-time full-field out of plane displacement data obtained using 3D DIC technique. Time instances were chosen to show the key features of the out of plane displacement process.

signal) with respect to time.

The out of plane displacement for both fillers obtained by 3D DIC technique is shown in Fig. 13. In Fig. 13, time = 0.0 ms is the instant when the shock wave reaches CH1 (no loading yet on the specimen). DIC contours at time = 1.4 and 4.1 ms show peaks in center point out

of plane displacements for both filler cases. However, a phase delay develops, and at time = 6.7 and 10.2 ms when the water cases are experiencing subsequent peaks in their center point deformations, the AMC cases are nearing minima in their center point deformations, indicating a divergence in their vibration frequencies. It is clearly seen in Fig. 13 that maximum out of plane displacement profiles for both fillers are similar in each case.

The out of plane displacement data obtained by 3D DIC technique for the center point data are presented in Fig. 14(a)–(c) and (b)–(d), respectively, for a quantitative representation. Fig. 14 shows that the maximum out of plane displacement for center point is quite similar for both liquid. It is also seen in Fig. 14 that the oscillation frequency of the out of plane displacement of the vibrating back-face plate is less with AMC filler than water filler. The oscillation frequency of the out of plane displacement is about 340 Hz with water filler while it is about 270 Hz with AMC filler in both Case#1 and #2, which shows that vibration of back face plate can still be damped 21% further via AMC than water. This considerably larger damping achieved by AMC filler can provide more dissipation of any undesirable energy input to the structure, a better prevention of the structural deformation, and a better restraining of resonant phenomena (keeping the natural and excitation frequencies unsynchronized) than water filler. Fig. 14 also shows the effect of the secondary loading presented in Fig. 12 on the out of plane displacement of the back-face plate. There is a secondary displacement peak in each experiment after 13 ms due to the secondary loading peak observed in Fig. 12. It is to be noted that among all the experiments conducted in the shock tube, the maximum principal strain on the PC back-face sheet was 0.93% for AMC-B-14.8, which is also within the elastic limits.

For the real-time out of plane displacement data presented in Fig. 14, a damping ratio (ζ) was obtained for the time period between 4 ms and 13 ms. This time period was chosen so as to avoid the first cycle when the response of the structure is forced by the shock loading. The damping ratio is given [50].

$$\zeta = \frac{1}{\sqrt{1 + \left(\frac{2\pi}{\delta}\right)^2}} \quad (2)$$

where δ is the logarithmic decrement, and given as

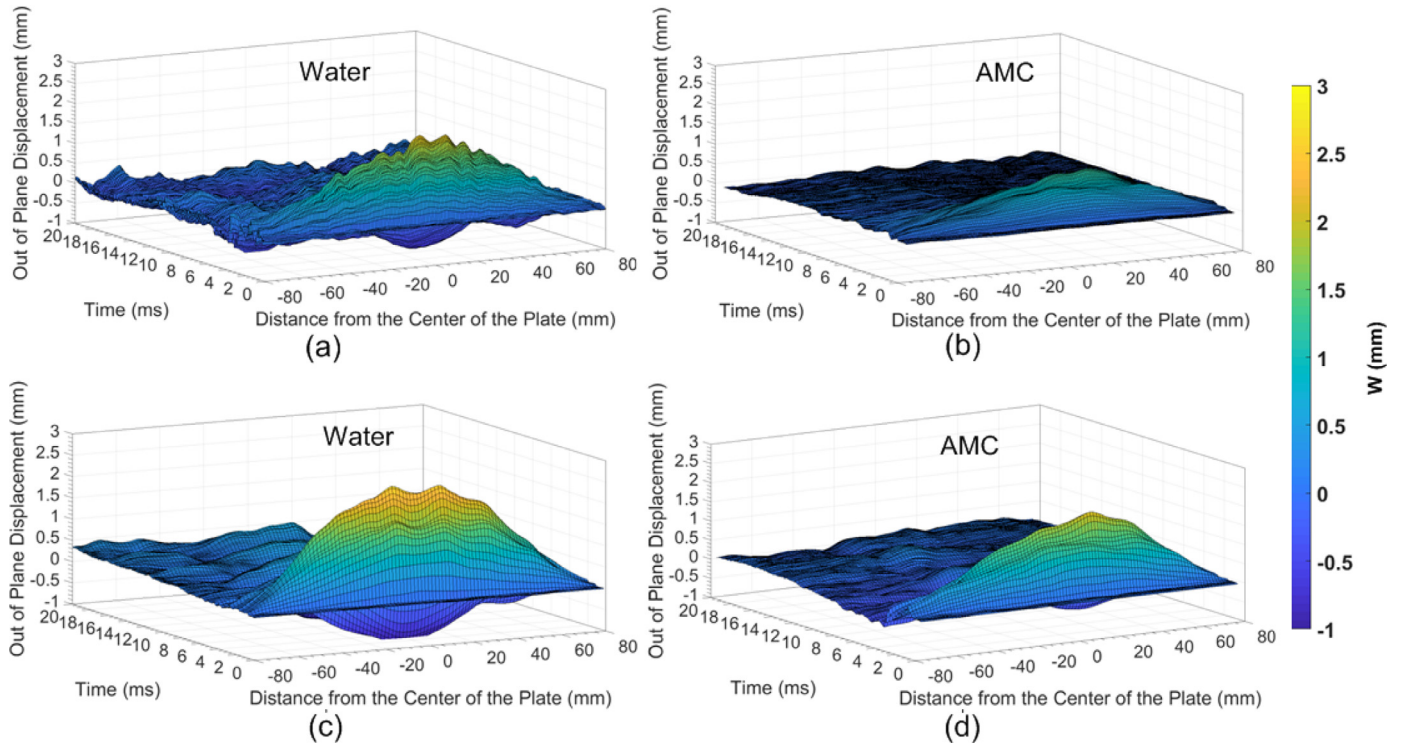


Fig. 10. The evolution of out of plane displacement data for a vertical line drawn along the center of the back-face plate (membrane) for (a)–(c) water and (b)–(d) AMC fillers (Case #1: (a) Water-A-1.4 and (b) AMC-A-1.4; Case #2: (c) Water-A-1.8 and (d) AMC-A-1.7).

$$\delta = \frac{1}{n} \ln \frac{x(t)}{x(t + nT)} \quad (3)$$

The damping ratios for AMC-B-14.8 and AMC-B-14.7 are calculated to be 0.113 and 0.122 while for Water-B-14.5 and Water-B-14.2 are calculated to be 0.080 and 0.082, respectively. The difference of ~45% in the magnitude of the damping ratio between AMC and water is evidence of a better mitigation performance of AMC. Similar damped response can be seen during the secondary loading for all the

Table 2

Experiments conducted by instrumented bar apparatus and their key results.

| Experiment | Input Impulse (N·s) | W_{\max} (mm) | Decrease in W_{\max} by AMCS (%) | U_{\max} (J) |
|-------------|---------------------|-----------------|------------------------------------|----------------|
| Water-A-1.4 | 1.4 | 2.18 | 40 | 0.12 |
| AMC-A-1.4 | 1.4 | 1.31 | | 0.08 |
| Water-A-1.8 | 1.8 | 2.68 | 20 | 0.37 |
| AMC-A-1.7 | 1.7 | 2.16 | | 0.28 |

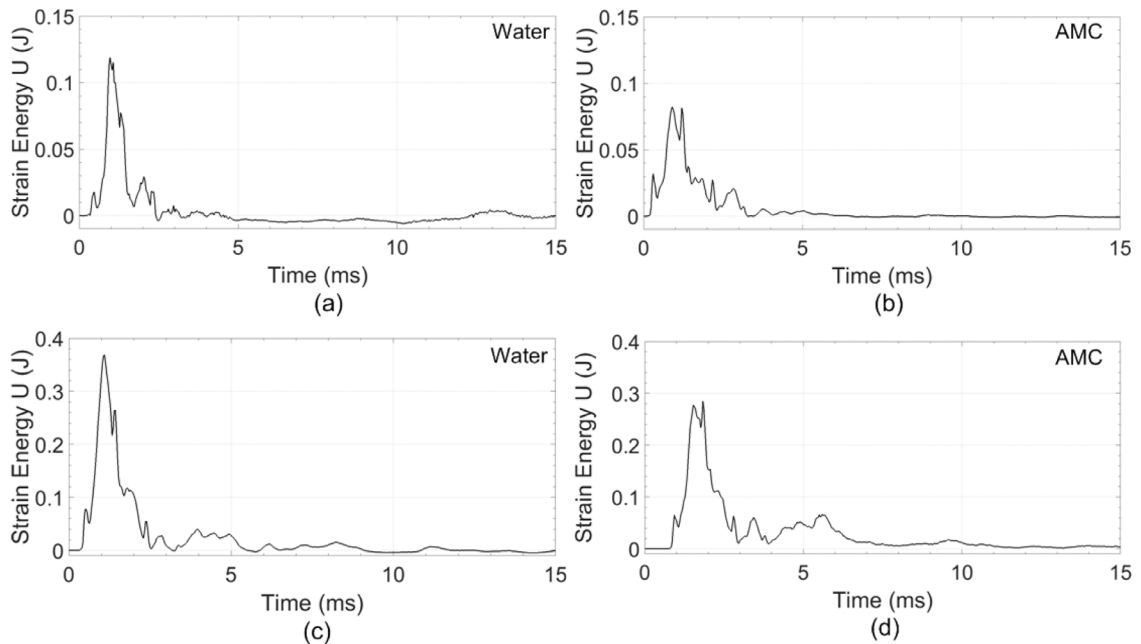


Fig. 11. The real-time full-field strain energy data obtained through 3D DIC technique (Case #1: (a) Water-A-1.4 and (b) AMC-A-1.4; Case #2: (c) Water-A-1.8 and (d) AMC-A-1.8).

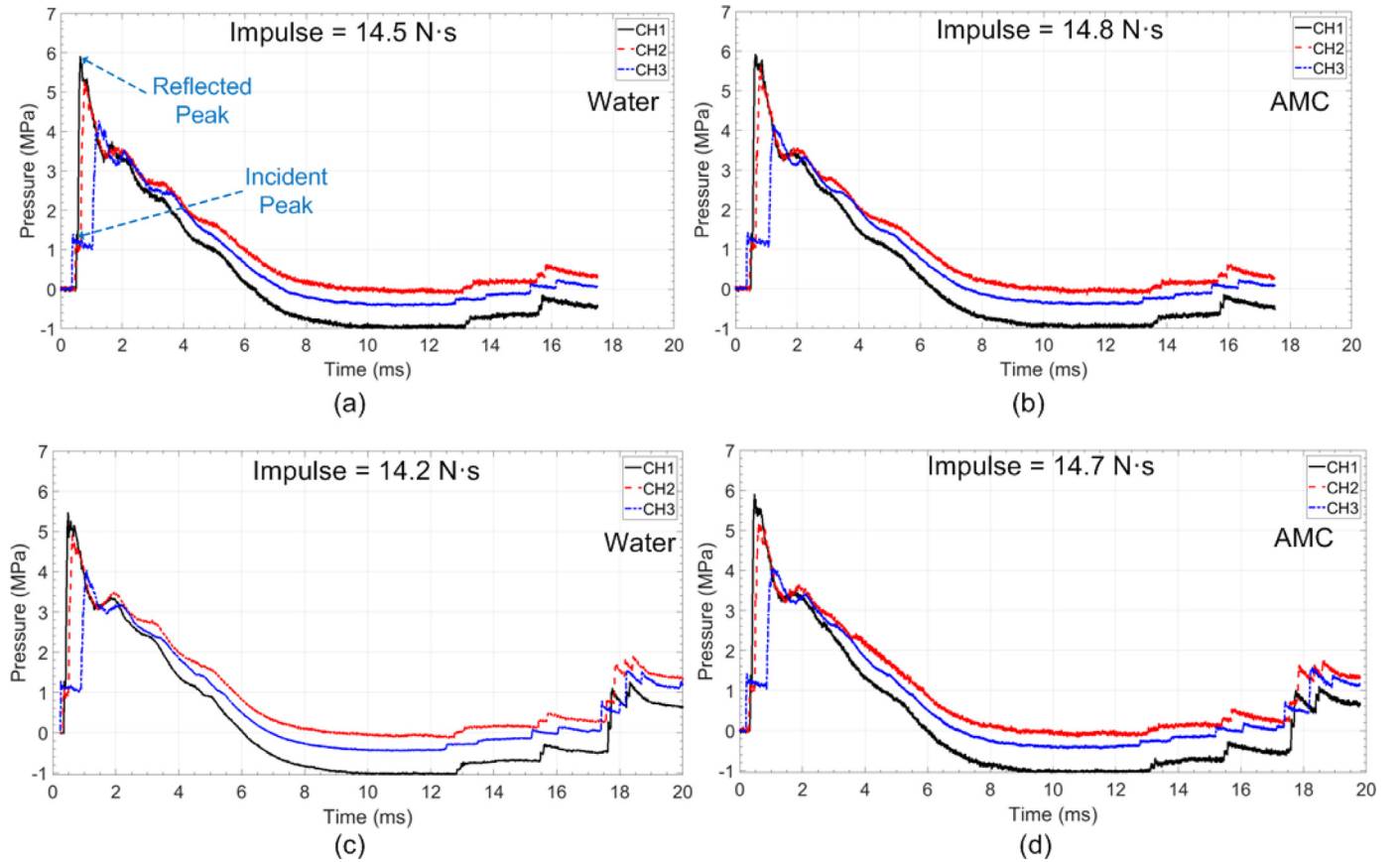


Fig. 12. Input pressures applied by the shock tube on the PC structure for (a)–(c) water and (b)–(d) AMC fillers (Case #1: (a) Water-B-14.5 and (b) AMC-B-14.8; Case #2: (c) Water-B-14.2 and (d) AMC-B-14.7).

experiments. However, it is to be noted that the shock tube experiments are not designed to collect any meaningful data for the successive loadings. As it is seen from Eq. (3) that there are two main parameters determining the magnitude of the logarithmic decrement, namely reduction in the peak displacement for the successive cycles and the number of cycles during the given time period. In the above cases, the number of cycles is the main driving parameter for the differences in the logarithmic decrement.

The evolution of the out of plane displacement data for a vertical line drawn along the center of the back-face plate is presented in Fig. 15. The smooth deflection curves for AMC seen in instrumented bar experiments are also seen for water in shock tube experiments as seen in Fig. 15.

The summary of all the key data from the shock tube experiments for each filler case is given in Table 3. Impulse is the impulse carried by the shock tube, W_{max} is the maximum out of plane displacement of the center point on the back-face plate, and f is the oscillation frequency of vibrating plate in Table 3.

3.3. Mechanical energy and power: Comparison between instrumented bar and shock tube setups

The instrumented bar experiments showed that AMC filler provides significantly better structural shock mitigation performance than water. On the other hand, the shock tube experiments showed that although AMC filler still provides significantly better mitigation performance than water, both liquid fillers provide similar maximum out of plane displacement response during the first monotonic loading. One can surmise that the observed difference in the maximum out of plane displacement response in each experimental configuration is due to the different loading rates applied by each setup. Fig. 16 shows a

comparison in the input forces applied by both instrumented bar and shock tube setups for AMC filler. It is seen in Fig. 16 that the rise time of the input force is $9.5 \mu s$ with a peak of 37.8 kN in instrumented bar experiment while it is $81 \mu s$ with a peak of 6.6 kN in shock tube experiment. So, the instrumented bar setup produces a loading rate 8.5 times faster than the shock tube. In the shock loading profile, there is a time delay between the real incident and reflected pulses acting on the structure due to the location of the pressure sensor (20 mm further from the structure). This was taken into account in the calculation of the rise time $81 \mu s$.

Incident energies for both instrumented bar [51] and shock loadings [46] can be now calculated from the experimental data, which are obtained to be 7.1 J (experiment (b) in Section 3.1) and 8.7 J (experiment (d) in Section 3.1) for instrumented bar experiments, and to be $16,284 \text{ J}$ (experiment (b) and (d) in Section 3.2) for shock tube experiments. The energy transmitted to AMC can be calculated through a straightforward impedance approach. Since the density and the speed of sound of each medium are known in this study, the reflection coefficient R can be calculated by [52]

$$R = \left(\frac{Z_2 - Z_1}{Z_2 + Z_1} \right)^2 \quad (4)$$

where Z_1 is the impedance of the transmitted medium and Z_2 is the impedance of the reflected medium. After finding the reflection coefficient R for each medium transition, the ratio of the transmission coefficient was calculated by subtracting R from 1. Then, multiplying the transmission coefficient with the respective energy gives the transmitted energy for AMC. Table 4 presents the transmitted energy to AMC, volume of AMC, ratio of the transmitted energy to AMC to volume of AMC, and applied energy rate (power) for both instrumented bar and shock tube loadings. More details of the energy calculation are

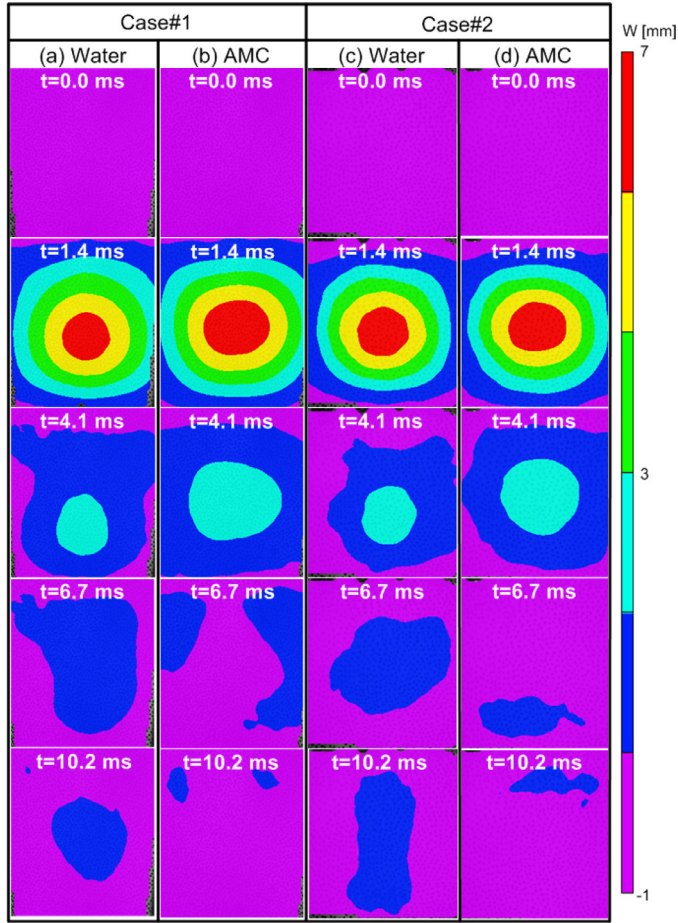


Fig. 13. The real-time full-field out of plane displacement data obtained through 3D DIC technique. Time instances were chosen as showing the key features of the out of plane displacement process.

provided in Appendix.

Table 4 shows that shock tube experiments impart about 3.4 times more energy to the liquid filler than the instrumented bar experiments. In both experiment types, if the total energy imparted to the liquid is divided by its total volume, the energy per mL obtained is considerably lower than threshold estimated in a previous report [33], which is 0.7 J per 1 mL of 5.6% wt. AMCS. However, we postulate the gelation upon impact within the layer is not homogenous throughout the entire volume of the liquid, and the present results show that for instrumented bar experiments considerable attenuation does occur, despite the provided energy per mL of solution, averaged out over the entire volume, being less one hundredths of the required amount – 0.0039 J/mL. One could therefore claim that the increased energy input per averaged mL solution in the shock tube experiments – 0.013 J/mL, should lead to more occurrences of local gelation and therefore better attenuation of the maximum out of plane displacement in these experiments. However, the opposite is the case, showing that these “total amount of energy” considerations are clearly insufficient, and the considerable difference in the AMCS attenuation performance on the maximum out of plane displacement between the two experimental systems should stem from a different cause. The rate of energy application to the solutions is 20 times higher in the instrumented bar system than in the shock tube system. It can consequently be inferred that this difference in rate (mechanical power) is crucial to the observed difference in the peak out of plane displacement response of the AMCS between the two loading setups. Based on this rate effect, it can be concluded that in the case of instrumented bar loading, stronger localized gelation of the AMCS occurs in sufficient time, thereby reducing the maximum out of plane displacement during the first cycle. However, in the case of shock tube, sufficient localized gelation of the AMCS occurs only after the first cycle.

4. Conclusion

In this work, the dynamic structural attenuation performance of AMC was examined by two loading techniques: Instrumented bar and shock tube. In both experiment types, the deflection of a back-face plate (Al or PC) protected by a layer of 5.6% AMC solution (94.4% water)

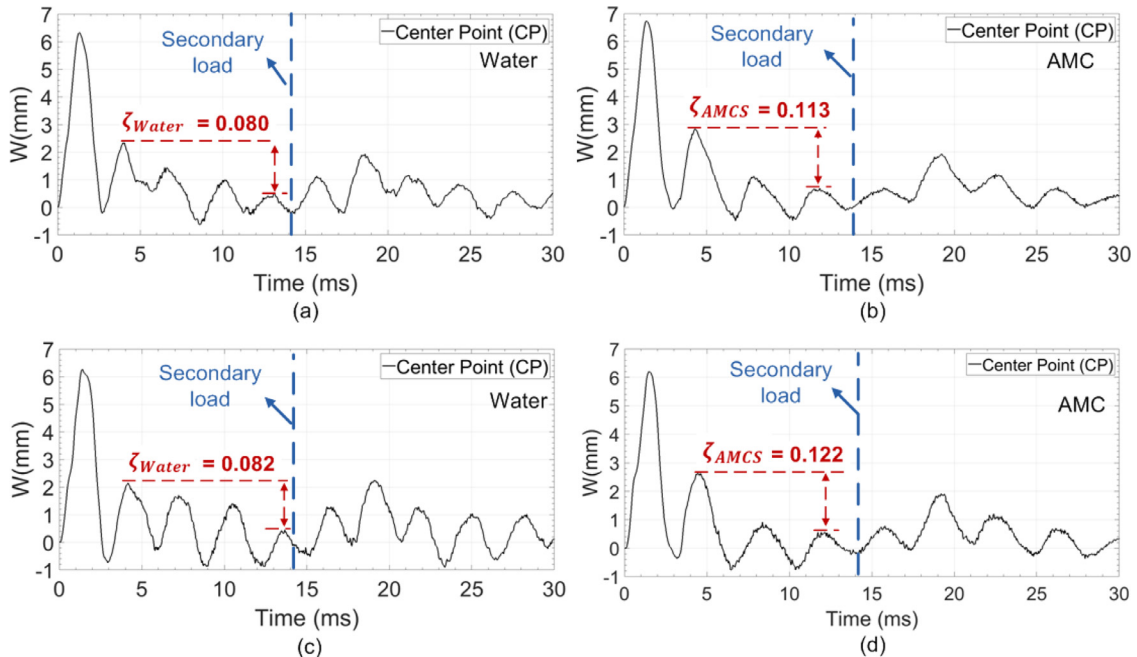


Fig. 14. The time variation of the real-time out of plane displacement data for the center point (where the maximum W occurs) of the back-face plate displacement (Case #1: (a) Water-B-14.5 and (b) AMC-B-14.8; Case #2: (c) Water-B-14.2 and (d) AMC-B-14.7).

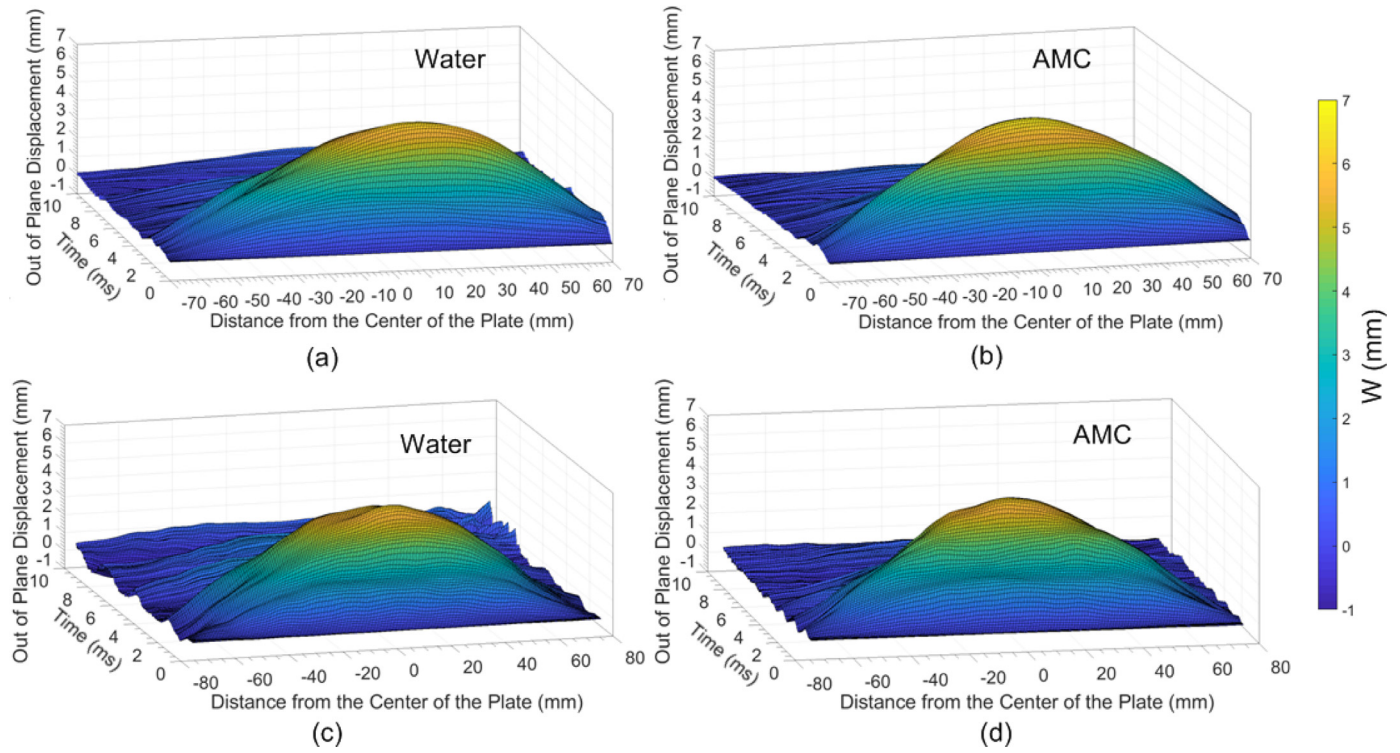


Fig. 15. The evolution of out of plane displacement data for a vertical line drawn along the center of the back-face plate for (a)–(c) water and (b)–(d) AMC fillers (Case #1: (a) Water-B-14.5 and (b) AMC-B-14.8; Case #2: (c) Water-B-14.2 and (d) AMC-B-14.7).

Table 3

Experiments conducted by shock tube apparatus and their key results.

| Experiment | Impulse (N·s) | W_{\max} (mm) | f (Hz) | Decrease in f by AMC (%) |
|--------------|---------------|-----------------|----------|----------------------------|
| Water-B-14.5 | 14.50 | 6.30 | 337 | 20 |
| AMC-B-14.8 | 14.80 | 6.70 | 270 | |
| Water-B-14.2 | 14.20 | 6.30 | 339 | 19 |
| AMC-B-14.7 | 14.70 | 6.20 | 273 | |

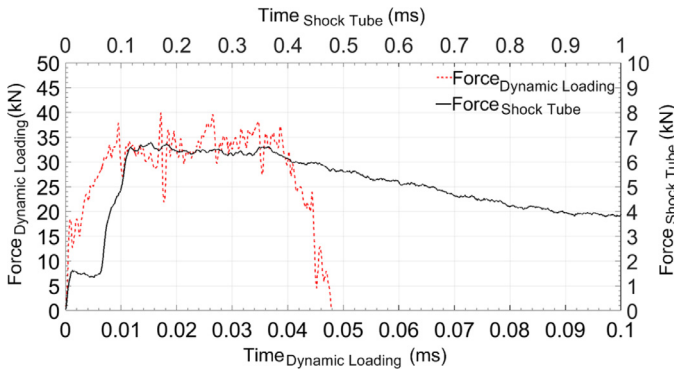


Fig. 16. Comparison of the input forces applied by both instrumented bar (red color) and shock tube (black color) setups. (For interpretation of the references to color in this figure legend, the reader is referred to the web version of this article.)

was measured to assess the shock transferred to the structure from the original impact.

Instrumented bar experiments have shown that in comparison to water, AMCS can reduce the maximum out-of-plane displacement by up to 40%. Results have also shown that the structural damping through AMC is significantly stronger than water. This performance can be crucial for structural protection. Instrumented bar experiments at

Table 4

The energy transmitted to AMC hydrogel in both instrumented bar and shock tube experiments.

| Experiment | Transmitted Energy, E_t (J) | V_{AMC} (ml) | E_t / V_{AMC} (J/ml) | \dot{E}_t (kW) |
|------------|-------------------------------|-----------------------|-------------------------------|------------------|
| AMC-A-1.4 | 2.2 | 692 | 0.0032 | 41.4 |
| AMC-A-1.7 | 2.7 | 692 | 0.0039 | 43.3 |
| AMC-B-14.8 | 9.1 | 692 | 0.0132 | 1.9 |
| AMC-B-14.7 | 9.1 | 692 | 0.0132 | 1.9 |

higher loading amplitudes have shown reduced efficiency, 20% of maximal out-of-plane displacement.

In contrast, shock tube experiments show similar peak out of plane displacement response in structures for both the liquids. We assume that in these cases, despite the larger amount of energy transmitted into the material from shock tube, the local endothermic phase transition fails to occur sufficiently during the first monotonic loading. We therefore surmise that the reason for this performance of the AMCS in the shock tube experiments is due to the lower loading rate, in other words lower mechanical power imparted to the AMCS. Also, the vibrations in the structures filled with AMCS occur at a much lower frequency compared to water filled structures due to a 45% reduction in damping ratio indicating a better mitigation performance of AMCS.

Although only 5.6% AMC solution was investigated in this work, AMC solutions with a higher weight percent have been observed to provide a better mitigation performance. However, increasing the weight percent in AMC solution may increase the viscosity of the solution making it difficult to compare results with pure water.

Thus, this study delineates the impact scenarios in which these commonly-found, non-toxic, and inexpensive materials, whose specific weight is similar to that of water, can serve as efficient mitigators of structural damage and vibrations.

CRediT authorship contribution statement

Koray Senol: Conceptualization, Methodology, Investigation, Visualization, Writing - original draft. **Galit Parvari:** Conceptualization, Methodology, Visualization, Writing - review & editing. **Yonatan Rotbaum:** Conceptualization, Methodology, Visualization, Writing - review & editing. **Yoav Eichen:** Conceptualization, Methodology, Supervision, Visualization, Writing - review & editing. **Daniel Rittel:** Conceptualization, Methodology, Supervision, Visualization, Writing - review & editing. **Arun Shukla:** Conceptualization, Methodology, Resources, Supervision, Visualization,

Writing - review & editing, Funding acquisition.

Acknowledgments

Koray Senol and Arun Shukla want to acknowledge Dr. Y.D.S. Rajapakse of the Office of Naval Research for providing the financial support under Grant no. N00014-17-1-2080. The support of the Department of Mechanical, Industrial and Systems Engineering, University of Rhode Island and the students from the Dynamic Photomechanics Laboratory is also gratefully acknowledged.

Supplementary materials

Supplementary material associated with this article can be found, in the online version, at [doi:10.1016/j.ijimpeng.2020.103547](https://doi.org/10.1016/j.ijimpeng.2020.103547).

Appendix

Energy calculations

The incident energy (presented in Section 3.3) for instrumented bar experiments are obtained using the following equation

$$E_{shpbi} = \int F_{shpbi} du_{shpb} \quad (5)$$

where E_{shpbi} is the input energy applied to the Al front face plate, F_{shpbi} is the input force applied to the Al front face plate (given in Fig. 1(a)), and u_{shpb} is the displacement of the Al front face plate (equal to the displacement of the dynamic loading bar) and can be obtained by

$$u_{shpb} = \int v_{shpb} dt \quad (6)$$

where v_{shpb} is the particle velocity in the dynamic loading bar, which can be obtained by [51]

$$v_{shpb} = c_{steel} (-\epsilon_i - \epsilon_r) \quad (7)$$

where c_{steel} is the longitudinal wave velocity in the dynamic loading bar, and ϵ_i and ϵ_r are the incident and the reflected strains collected through the strain gages attached to the dynamic loading bar, respectively. Then, the energy transmitted to the AMC (given in Table 4) can be calculated by

$$E_{shpbt} = (1 - R_{Al}) E_{shpbi} \quad (8)$$

where E_{shpbt} is the transmitted energy to the AMC and R_{Al} is the reflection coefficient for Al and can be calculated from Eq. (4). Then, the loading rate of the transmitted energy (given in Table 4) can be calculated by

$$\dot{E}_{shpbt} = \frac{\Delta E_{shpbt}}{\Delta t} \quad (9)$$

The incident energy (presented in Section 3.3) for shock tube experiments are obtained as following [46]

$$E_{sti} = \int S v_{sti} \left(\frac{\gamma P_{sti}}{\gamma - 1} + 0.5 \rho_{sti} v_{sti}^2 \right) dt \quad (10)$$

where E_{sti} is the incident energy that the shock tube carries, S is the cross sectional area of the shock tube muzzle, v_{sti} is the particle velocity, γ is the adiabatic exponent of the gas constant, P_{sti} is the incident pressure, ρ_{sti} is the density of the gas. Then, the energy transmitted to the AMC (given in Table 4) can be calculated by

$$E_{stt} = (1 - R_{air})(1 - R_{PC}) E_{sti} \quad (11)$$

where E_{stt} is the transmitted energy to the AMC and R_{air} and R_{PC} are the reflection coefficients for air and PC front face plate, respectively, and can be calculated from Eq. (4). The loading rate of the transmitted energy (given in Table 4) can be calculated by

$$\dot{E}_{stt} = \frac{\Delta E_{stt}}{\Delta t} \quad (12)$$

Table 5 summarizes the values of the key data used in the calculation of the transmitted energy for both instrumented bar and shock tube experiments.

Table 5

The values of the key data used in the calculation of the transmitted energy for both instrumented bar and shock tube experiments.

| Experiment | c_{steel} (m/s) | R_{Al} | Δt (ms) | S (mm ²) | v_{sti} (m/s) | γ | ρ_{sti} (kg/m ³) | R_{air} | R_{PC} |
|------------|-------------------|----------|-----------------|------------------------|-----------------|----------|-----------------------------------|----------------|----------|
| SHPB | 5790 | 0.6863 | 0.054 | N/A | N/A | N/A | N/A | N/A | N/A |
| Shock Tube | N/A | N/A | 4.668 | 1134 | 1140 | 1.35 | 0.44 | 0.9994 [53–55] | 0.0645 |

References

- [1] Budynas RG, Nisbett JK. Shigley's mechanical engineering design. New York: McGraw-Hill; 2008.
- [2] Kaliszky S, Logo J. Optimal design of elasto-plastic structures subjected to normal and extreme loads. *Comput Struct* 2006;84(28):1770–9.
- [3] Ngo T, Mendis P, Gupta A, Ramsay J. Blast loading and blast effects on structures—an overview. *Electron J Struct Eng* 2007;7(S1):76–91.
- [4] Helmore E. US Air Force prepares drones to end era of fighter pilots. *The UK Guardian*; 2009.
- [5] Hassanalian M, Abdelkefi A. Classifications, applications, and design challenges of drones: a review. *Prog Aerosp Sci* 2017;91(99–131).
- [6] G.B. Engelhardt, "High-g centrifuge," 1949.
- [7] R.J. Wojnarowski and C.W. Eichelberger, "Electronic systems disposed in a high force environment," 1993.
- [8] B. Miller, "Wave slamming on offshore structures," 1980.
- [9] Ren B, Wang Y. Numerical simulation of random wave slamming on structures in the splash zone. *Ocean Eng* 2004;31(5–6):547–60.
- [10] Rausa IE, Muskulus M, Arntsen Ø, Wåsjø K. Characterization of wave slamming forces for a truss structure within the framework of the WaveSlam project. *Energy Procedia* 2015;80:276–83.
- [11] Rijensky O, Rittel D. Polyurea coated aluminum plates under hydrodynamic loading: does side matter? *Int J Impact Eng* 2016;98:1–12.
- [12] Faltinsen OM, Landrini M, Greco M. Slamming in marine applications. *J Eng Math* 2004;48(3–4):187–217.
- [13] L. Groesch, G. Netzer, and L. Kassing, "Dummy for car crash testing," 1987.
- [14] J. Foster, J. Kortge, and M. Wolanin, "Hybrid III-A biomechanically-based crash test dummy," 1977.
- [15] Mukai T, Kanahashi H, Higashi K, Miyoshi T, Mabuchi M, Nieh T. Experimental study of energy absorption in a close-celled aluminum foam under dynamic loading. *Scr Mater* 1999;40(8).
- [16] Cui L, Kiernan S, Gilchrist MD. Designing the energy absorption capacity of functionally graded foam materials. *Mater Sci Eng A* 2009;507(1–2):215–25.
- [17] Yeoh O. Some forms of the strain energy function for rubber. *Rubber Chem Technol* 1993;66(5):754–71.
- [18] Alghamdi A. Collapsible impact energy absorbers: an overview. *Thin-Walled Struct* 2001;39(2):189–213.
- [19] Rahimzadeh T, Arruda EM, Thouless M. Design of armor for protection against blast and impact. *J Mech Phys Solids* 2015;85:98–111.
- [20] Ahmed EM. Hydrogel: preparation, characterization, and applications: a review. *J Adv Res* 2015;6(2):105–21.
- [21] Guilherme MR, et al. Superabsorbent hydrogels based on polysaccharides for application in agriculture as soil conditioner and nutrient carrier: a review. *Eur Polym J* 2015;72:365–85.
- [22] Hoare TR, Kohane DS. Hydrogels in drug delivery: progress and challenges. *Polymer (Guildf)* 2008;49(8):1993–2007.
- [23] Shewan HM, Stokes JR. Review of techniques to manufacture micro-hydrogel particles for the food industry and their applications. *J Food Eng* 2013;119(4):781–92.
- [24] Kashyap N, Kumar N, Kumar MNVR. Hydrogels for pharmaceutical and biomedical applications. *Crit Rev Ther Drug Carrier Syst* 2005;22(2):107–50.
- [25] Drury JL, Mooney DJ. Hydrogels for tissue engineering: scaffold design variables and applications. *Biomaterials* 2003;24(24):4337–51.
- [26] Kamoun EA, Kenawy ERS, Chen X. A review on polymeric hydrogel membranes for wound dressing applications: PVA-based hydrogel dressings. *J Adv Res* 2017;8(3):217–33.
- [27] Kobayashi K, Huang C-I, Lodge TP. Thermoreversible gelation of aqueous methylcellulose solutions. *Macromolecules* 1999;32(21):7070–7.
- [28] Sarkar N. Thermal gelation properties of methyl and hydroxypropyl methylcellulose. *J Appl Polym Sci* 1979;24(4):1073–87.
- [29] Thirumala S, Gimble J, Devireddy R. Methylcellulose based thermally reversible hydrogel system for tissue engineering applications. *Cells* 2013;2(3):460–75.
- [30] Pakulska MM, Vulic K, Tam RY, Shoichet MS. Hybrid crosslinked methylcellulose hydrogel: a predictable and tunable platform for local drug delivery. *Adv Mater* 2015;27(34):5002–8.
- [31] Chen YC, Chen YH. Thermo and pH-responsive methylcellulose and hydroxypropyl hydrogels containing K₂SO₄ for water retention and a controlled-release water-soluble fertilizer. *Sci Total Environ* 2019;655:958–67.
- [32] Nasatto PL, Pignon F, Silveira JL, Duarte MER, Noseda MD, Rinaudo M. Methylcellulose, a cellulose derivative with original physical properties and extended applications. *Polymers (Basel)* 2015;7(5):777–803.
- [33] Parvari G, Rotbaum Y, Eichen Y, Rittel D. Impact-induced gelation in aqueous methylcellulose solutions. *Chem Commun* 2018;54(89):12578–81.
- [34] Wang Q, Li L. Effects of molecular weight on thermoreversible gelation and gel elasticity of methylcellulose in aqueous solution. *Carbohydr Polym* 2005;62(3):232–8.
- [35] Lam Y, Joshi SC, Tan BK. Thermodynamic characteristics of gelation for methylcellulose hydrogels. *J Therm Anal Calorim* 2007;87(2):475–82.
- [36] Wang Z, Yang K, Li H, Yuan C, Zhu X, Huang H. In situ observation of gelation of methylcellulose aqueous solution with viscosity measuring instrument in the diamond anvil cell. *Carbohydr Polym* 2018;190(September 2017):190–5.
- [37] Su L, Wang Z, Yang K, Minamikawa Y, Kometani N, Nishinari K. In situ observation of heat-and pressure-induced gelation of methylcellulose by fluorescence measurement. *Int J Biol Macromol* 2014;64:409–14.
- [38] Rotbaum Y, Parvari G, Eichen Y, Rittel D. Mechanical reinforcement of methylcellulose hydrogels by rigid particle additives. *Mech Mater* 2019;132:57–65.
- [39] Rotbaum Y, Parvari G, Eichen Y, Rittel D. Linear and non linear shock attenuation of aqueous methylcellulose solutions. *Int J Impact Eng* 2019(xxxx).
- [40] Petersen R, Link R, Gomez J, Shukla A. Static and dynamic behavior of damaged concrete and granite in compression. *J Test Eval* 2009;29(6):563.
- [41] Gomez JT, Shukla A, Sharma A. Static and dynamic behavior of concrete and granite in tension with damage. *Theor Appl Fract Mech* 2001;36(1):37–49.
- [42] Sutton MA, Orteu J-J, Schreier HW. *Image correlation for shape, motion and deformation measurements*. 2009.
- [43] Senol K, Shukla A. Underwater mechanical behavior of closed cell PVC foams under hydrostatic loading through 3D DIC technique. *Polym Test* 2019;73.
- [44] Senol K, Shukla A. Dynamic response of closed cell PVC foams subjected to underwater shock loading. *Int J Impact Eng* 2019.
- [45] Wu X, et al. Reversible hydrogels with tunable mechanical properties for optically controlling cell migration. *Nano Res* 2018;11(10):5556–65.
- [46] Wang E, Shukla A. Analytical and experimental evaluation of energies during shock wave loading. *Int J Impact Eng* 2010;37:1188–96.
- [47] Kolsky H. An investigation of the mechanical properties of materials at very high rates of loading. *IOP Publ* 1949;62:676.
- [48] Chen W, Song B. *Split Hopkinson (Kolsky) bar: design, testing and applications*. Springer; 2011.
- [49] Rajendran R, Narasimhan K. Linear elastic shock response of plane plates subjected to underwater explosion. *Int J Impact Eng* 2001;25:493–506.
- [50] Meirovitch L. fundamentals of vibrations. McGraw-Hill; 2001.
- [51] Shukla A, Dally JW. *Experimental solid mechanics*. Knoxville, TN: College House Enterprises; 2014.
- [52] Kim Y-H. Sound propagation. John Wiley & Sons; 2010. p. 2010.
- [53] Hosseini H, Moosavi-Nejad S, Akiyama H, Menezes V. Shock wave interaction with interfaces between materials having different acoustic impedances. *Appl Phys Lett* 2014;104(10).
- [54] Baird J. Explosive shocks and impedance mismatch in armatures. *Electromagn Phenom* 2003;3:405–13.
- [55] Holfeld J, Tepeköylü C, Kozaryn R, Mathes W, Grimm M, Paulus P. Shock wave application to cell cultures. *J Vis Exp* 2014(86).